

## Three-dimensional *ab initio* description of vibration-assisted electron knock-on displacements in graphene

Alexandru Chirita <sup>1,2</sup>, Alexander Markevich,<sup>1</sup> Mukesh Tripathi <sup>1,\*</sup>, Nicholas A. Pike <sup>3</sup>, Matthieu J. Verstraete <sup>3</sup>,  
Jani Kotakoski <sup>1</sup> and Toma Susi <sup>1,†</sup>

<sup>1</sup>University of Vienna, Faculty of Physics, Boltzmannngasse 5, 1090 Vienna, Austria

<sup>2</sup>University of Vienna, Vienna Doctoral School in Physics, Boltzmannngasse 5, 1090 Vienna, Austria

<sup>3</sup>nanomat/Q-MAT/CESAM and European Theoretical Spectroscopy Facility,  
Université de Liège, B-4000 Liège, Belgium



(Received 18 November 2021; revised 6 April 2022; accepted 12 May 2022; published 13 June 2022)

Transmission electron microscopy characterization may damage materials, but an electron beam can also induce interesting dynamics. Elastic knock-on is the main electron irradiation damage mechanism in metals including graphene, and although atomic vibrations influence its cross section, only the out-of-plane direction has been considered so far. Here, we present a full three-dimensional first-principles theory of knock-on displacements including the effect of temperature on vibrations to describe dynamics into arbitrary directions. We validate the model with previously precisely measured knock-on damage of pristine graphene, where we show that the isotropic out-of-plane approximation correctly describes the cross section. We then apply our methodology to reversible jumps of pyridinic nitrogen atoms, whose probability under irradiation is measured at 55 and 60 keV. Direct displacement requiring a high emission angle and an alternative pathway via intermittent N adatom creation and recombination are computationally explored but are unable to explain the observed rates, implying stronger inelastic effects at the defect than in pristine graphene.

DOI: [10.1103/PhysRevB.105.235419](https://doi.org/10.1103/PhysRevB.105.235419)

### I. INTRODUCTION

Transmission electron microscopy (TEM) is a powerful probe of the atomic structure of materials. Due to efficient aberration correction [1], the information that modern instruments can collect is mainly limited by radiation damage [2], which can have both elastic and inelastic components. Knock-on displacement due to elastic electron backscattering [3] affects all materials and is the primary damage mechanism for metals such as graphene [4]. For nondestructive imaging, the electron should not transfer more energy than the displacement threshold of the material, defined as the energy needed to remove an atom from its lattice position. The energy received by the nucleus may also drive certain nondestructive dynamics [5,6], which has enabled atomically precise manipulation [7–9].

Since the electron mass is small compared to the nuclei, momentum conservation strictly limits the amount of kinetic energy transferred in an elastic collision. However,

at low electron energies, the thermal motion of the atom can significantly increase the energy transfer [10], and irradiation damage of graphene at energies below 100 keV cannot be explained without vibrations [11]. To date, these have only been treated in the out-of-plane direction of the greatest momentum transfer. For a complete description of situations including the beam-induced movement of adatoms [12], momentum transfers in all directions must be included. Furthermore, while knock-on damage in pristine graphene can be accurately described from first principles [13,14], there are puzzling discrepancies between the predicted and measured cross sections for its impurity sites [15]. Until now, it has not been clear whether these are due to shortcomings in the elastic model or arise from unaccounted inelastic effects.

We present here a full three-dimensional theory of electron knock-on damage for arbitrarily moving target atoms, which can be used in general to predict the probabilities of elastic processes based solely on first-principles modeling. We explore the implications of the theory for knock-on displacements from pristine graphene as well as for the reversible transformations of its pyridinic nitrogen impurity sites [16], for which we include new quantitative measurements. We explore both a direct pathway that can only be activated for primary knock-on atom emission directions close to the plane and also the possibility of intermittent N adatom creation and recombination in contributing to the observed dynamics. This provides a particularly demanding test of our *ab initio* framework, and although elastic theory fails in this instance, it

\*Present address: École Polytechnique Fédérale de Lausanne (EPFL), BM 2143, Station 17, CH-1015 Lausanne, Switzerland.

†toma.susi@univie.ac.at

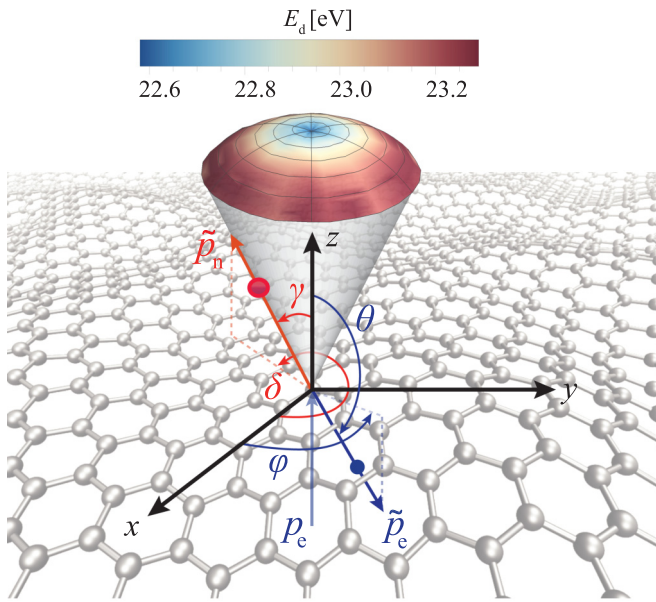


FIG. 1. The three-dimensional electron-atom scattering geometry.  $\varphi$  and  $\theta$  are the azimuthal and polar electron scattering angles after the collision (blue), whereas  $\delta$  and  $\gamma$  are the azimuthal and polar emission angles of the atom (red). The colored dome indicates the calculated and interpolated angular variation of the displacement threshold energy  $E_d$  for pristine graphene (multiplied by  $\xi = 0.931$  to match the experimental cross section; see Table I).

is applicable for the quantitative description of pure knock-on displacements more generally.

## II. ENERGY TRANSFER

To construct a three-dimensional model, we consider the electron (mass  $m$ , energy  $E_e$ , momentum  $p_e$ ) as a relativistic projectile scattering from a moving, nonrelativistic target, the nucleus (mass  $M$ , energy  $E_n$ , momentum  $p_n$ ). Assuming an initial electron momentum along the  $z$  axis,

$\mathbf{p}_e = |\mathbf{p}_e|(0, 0, 1)$  with  $|\mathbf{p}_e| = p_e = \sqrt{E_e(E_e + 2mc^2)}/c^2$  ( $c$  is the speed of light), and that the targeted atom has initial momentum components in three Cartesian directions  $\mathbf{p}_n = M(v_x, v_y, v_z)$ , where  $v_{x,y,z}$  are the initial nuclear velocity, we derive a three-dimensional description of the electron-nucleus scattering (Fig. 1 illustrates the geometry). The electron can scatter into any angle after the collision,  $\tilde{\mathbf{p}}_e = |\tilde{\mathbf{p}}_e|(\sin\theta \cos\varphi, \sin\theta \sin\varphi, \cos\theta)$ , and so can the atom,  $\tilde{\mathbf{p}}_n = |\tilde{\mathbf{p}}_n|(\sin\gamma \cos\delta, \sin\gamma \sin\delta, \cos\gamma)$ , where  $\varphi$  and  $\theta$  are the electron azimuthal and polar scattering angles and  $\delta$  and  $\gamma$  are the corresponding atom emission angles.

To provide a starting point for the simulation of the resulting dynamics, we are interested in the energy transferred to the nucleus  $\tilde{E}_n$ . This can be derived from the relativistic energy and momentum conservation of the incoming electron and the nucleus (this analytic solution assumes that  $E_e \gg \tilde{E}_n - E_n$ ; see the Supplemental Material [17] for details):

$$\begin{aligned} \tilde{E}_n(E_e, v_{x,y,z}, \theta, \varphi) = & \frac{M(v_x^2 + v_y^2 + v_z^2)}{2} \\ & + p_e \left[ \frac{(1 - \cos\theta)(p_e + Mv_z)}{M} \right. \\ & \left. - \sin\theta(v_x \cos\varphi + v_y \sin\varphi) \right]. \end{aligned} \quad (1)$$

Note that although electron scattering from the Coulomb potential of the nucleus is spherically symmetric, the inclusion of arbitrary velocity components breaks that symmetry for atom emission. While Eq. (1) provides the general expression of energy transfer in terms of the electron scattering angles  $\varphi$  and  $\theta$ , a connection to the atom emission angles  $\gamma$  and  $\delta$  is needed to describe its displacement after the collision, which is what can be directly simulated [5,18]. These emission angles can be derived from momentum conservation ([17]; Fig. 1 again shows the geometry); note that  $\gamma$  and  $\delta$  now depend on the instantaneous velocity of the atom at the moment of the scattering, and yield unique values for any specific initial state:

$$\gamma(E_e, v_{x,y,z}, \theta, \varphi) = \arctan \left( \frac{\sqrt{(Mv_x - p_e \sin\theta \cos\varphi)^2 + (Mv_y - p_e \sin\theta \sin\varphi)^2}}{Mv_z + p_e(1 - \cos\theta)} \right), \quad (2)$$

$$\delta(E_e, v_{x,y,z}, \theta, \varphi) = \arctan \left( \frac{Mv_y - p_e \sin\theta \sin\varphi}{Mv_x - p_e \sin\theta \cos\varphi} \right). \quad (3)$$

## III. MODELING THE CROSS SECTION

To estimate the displacement threshold energy for knock-on from pristine graphene, we ran density functional theory molecular dynamics (DFT/MD) simulations using our established methodology [6,13] for atom emission angles  $0^\circ \leq \gamma \leq 30^\circ$  (as reduced energy transfer to larger angles cannot overcome the displacement threshold energy  $E_d$  [17]) and  $0^\circ \leq \delta \leq 60^\circ$ , which by symmetry allows us to predict  $E_d(\gamma, \delta)$  for all azimuthal angles. We used the Atomic Simulation Environment [19] for Velocity-Verlet dynamics with a time step of 0.3 fs on a  $7 \times 7 \times 1$  graphene supercell, with forces from a GPAW [20] DFT calculator using the PBE

functional [21], a  $dzp$  basis set, a  $3 \times 3 \times 1$  Monkhorst-Pack  $\mathbf{k}$ -point grid, and a Fermi-Dirac smearing of 0.025 eV (which results in ca. 0.6 eV higher values of  $E_d$  than the previously used default setting of 0.1 eV [13]).  $E_d$  increases for emission angles  $\gamma > 0^\circ$ , as shown in Fig. 1 (and noted earlier [22]). Combined with the fact that a normally incident electron can transfer less energy the larger the angle  $\gamma$  is, this illustrates why the out-of-plane approximation has worked well for this typical geometry.

In experimental studies, only the rate of displacements at a given irradiation dose can be measured, from which the cross section for each electron impinging on an atom can be

TABLE I. Different cross-section models describing experimental data for carbon displacement from  $^{12}\text{C}$  graphene and the pyridinic N jump (N-C<sub>2</sub>). “z-only” corresponds to the  $v_z$ -dependent cross section  $\sigma_z$  with an isotropic threshold energy  $E_d$  [13,14] while “3D” refers to the 3D cross section  $\sigma_{3D}$  with the nonisotropic threshold energy  $E_d(\gamma, \delta)$ . Only the lowest  $E_d$  values with the corresponding lowest emission angles are listed here; see Fig. 1 and Ref. [17] for their full 3D variation.  $\xi$  is a fitting factor for the simulated displacement threshold energies used to match the experimental displacement cross sections (for pristine graphene from Ref. [13] and for pyridinic N shown in Fig. 3), and WSME is the weighted mean-squared error minimized by the fitting. For the cross sections from adatom recombination, we give values based on the estimated probability of the N atom to be recaptured on the other side (47%).

System $\sigma$ model	Graphene		N jump		N adatom 47%	
	z-only	3D	z-only	3D	z-only	3D
$\xi$	0.932	0.938	0.167	0.224	0.629	0.579
$E_d$ [eV] ( $\gamma, \delta$ )	22.55 (0°, 0°)		13.00 (55°, 90°)		16.0 (0°, 0°)	
WMSE	0.005	0.004	1.18	0.55	198	94.2
Ref.	[13]		this work			

calculated and compared to theoretical estimates. Electrons displace atoms via Coulomb interaction with the nuclei, and the relativistic scattering cross section between an electron and a target atom has been derived by Mott [23] and expanded by McKinley and Feshbach [24] to obtain an analytical expression  $\sigma(E_e, \theta)$  [17], accurate up to middle-Z elements. Defect creation in pristine graphene starts a few tens of keV below the primary beam energy  $E_e$  that is needed to overcome  $E_d$  in a static lattice approximation, explained by accounting for the vibrational enhancement of the momentum transfer [11]. Most calculations have assumed that  $E_d$  is isotropic [25], and that only out-of-plane vibrations (if any) are important [13]. We expand the theory to a fully three-dimensional model including vibrations and momentum transfer in arbitrary directions, giving the cross section  $\sigma_{3D}$  as an integral over the electron scattering angles and the nuclear velocity components [17]:

$$\sigma_{3D}(E_e, E_d, T) = \int_0^{2\pi} \int_0^\pi \prod_{i=x,y,z} \int_{-v_i^{\max}}^{v_i^{\max}} P(v_i, \overline{v_i^2}(T)) \mathcal{H}(\tilde{E}_n - \xi E_d(\gamma, \delta)) \sigma(E_e, \theta) dv_i \sin \theta d\theta d\varphi, \quad (4)$$

where  $P(v_i, \overline{v_i^2}(T))$  with  $i = x, y, z$  are the normal distributions of Cartesian atom velocities with mean-square widths  $\overline{v_i^2}(T)$  derived from the phonon density of states and integrated over  $\pm v_i^{\max}$  covering their variation [13], and  $\mathcal{H}$  is a Heaviside step function ensuring the transferred energy  $\tilde{E}_n$  [Eq. (1)] exceeds the value of the angle-dependent displacement threshold  $E_d(\gamma, \delta)$  [17]. The latter may need to be multiplied by a fitting factor  $\xi$  to match the experimental cross section (see Table I). This demanding five-dimensional expression could only be integrated using adaptive numerical methods [17].

We further considered the pyridinic N site (N-C<sub>2</sub>), which is similar to a single vacancy, but with the dangling-bond C atom replaced by N, bonding to two C neighbors and stabilizing the defect. These N impurities have been observed to rapidly “jump” back and forth across the vacancy under electron irradiation at 500 °C [16]. The calculated energy barrier of  $\sim 4$  eV for the process is too high to be thermally activated, but neither was it possible to explain the observed event rate with the earlier models [15]. Since the predicted minimum-energy

pathway is in-plane [26], the in-plane velocities  $v_{x,y}$  were presumed to play a role in activating the jumps.

We ran DFT/MD for various emission angles at the N-C<sub>2</sub> site to determine under which conditions the N can cross the vacancy to bind with the C atoms on the other side. Using phonon modeling via first-principles calculations [17] following our earlier methodology [9], we estimated mean-squared velocities of  $\{\overline{v_x^2} = 4.81, \overline{v_y^2} = 3.72, \text{ and } \overline{v_z^2} = 2.14\} \times 10^5 \text{ m}^2 \text{ s}^{-2}$  for the N atom (where the  $y$  direction points across the vacancy) to quantify the effect of its in- and out-of-plane motion.

Maximum energy transfers near electron backscattering do not result in a jump, regardless of the initial momentum of the N atom. Instead, effective emission directions lie in a narrow sector between  $90^\circ \leq \delta \leq 110^\circ$  (and symmetrically toward the other side, where  $\delta = 90^\circ$  points directly across the vacancy) and at relatively large polar emission angles  $55^\circ \leq \gamma \leq 90^\circ$ , with  $E_d^N(\gamma, \delta)$  ranging from 10 to 13.5 eV [Fig. 2(a)]. We interpolated the resulting threshold values and calculated cross sections with Eq. (4). However, we had to drastically scale down  $E_d(\gamma, \delta)$  with the multiplicative factor  $\xi$  [see Fig. 2(b) and Table I] so that the N could receive sufficient energy to reach the other side of the vacancy against the restoring force from its two original C neighbors.

For other angles or energies, either no change in the site occurs, or the N almost ejects from the lattice and is left as an adatom near its original position, which happens for a range of emission angles close to the surface normal at energies between 14–16 eV [Fig. 2(c)]. Although most such adatom configurations presumably recombine at the closest side of the defect, thus restoring the site to its original configuration, adatom migration at room temperature may allow some of them to recombine on the other side, which would be experimentally indistinguishable from a direct jump. At even higher transferred energies, which are increasingly unlikely at primary beam energies of 60 keV or below, the N can be entirely ejected from the lattice.

To evaluate the probability of an adatom recombining on either the original side of the vacancy, or the other side thus appearing as a jump, we ran Monte Carlo simulations in three simulation cells: an open world, where an adatom can diffuse away from the defect, and closed periodic cells of two sizes modeling the potential energy well around the vacancy, where it always ends up recombining on either side. These constitute

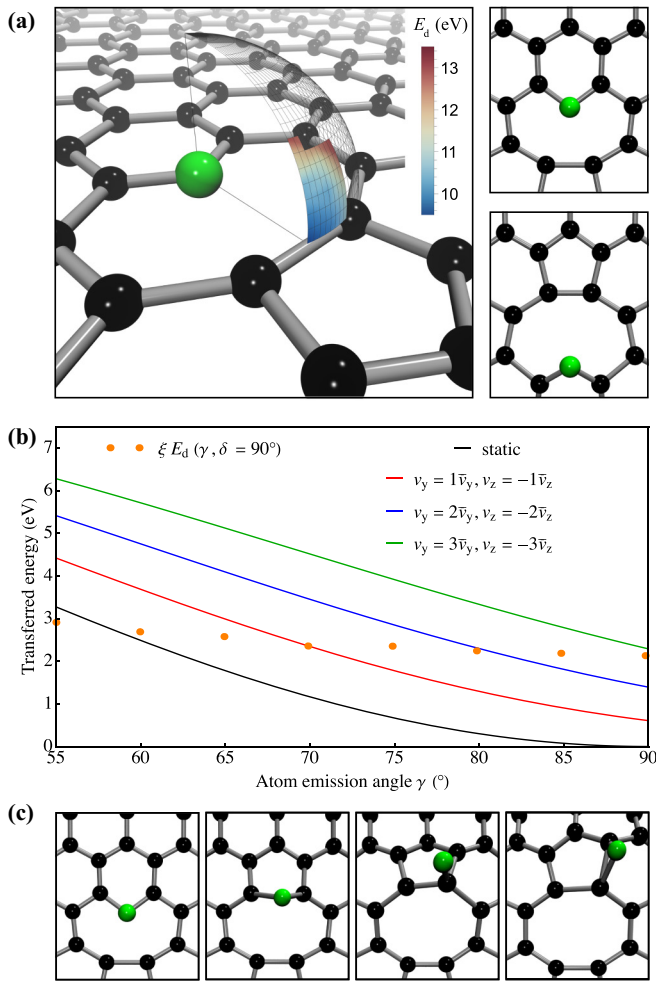


FIG. 2. Mechanisms of the N-C<sub>2</sub> dynamics. (a) Variation of the threshold energy  $E_d(\gamma, \delta)$  for the jumping of the N atom (shown in green) estimated with DFT/MD and numerically interpolated. The direction across the vacancy parallels the positive  $y$  axis ( $\delta = 90^\circ$ ). The coloring of each angular tile displays a numerical interpolation between the  $E_d$  values spanning its angular range, while the uncolored tiles represent directions where no jump is found. The top views show the initial and final snapshots from a DFT/MD simulation ( $\gamma = 60^\circ$ ,  $\delta = 90^\circ$ ,  $\vec{E}_n = 10$  eV). (b) Scaled  $\xi E_d$  (orange circles;  $\xi = 0.224$ ) compared to transferred energies as a function of polar atom emission angle  $\gamma$  and 3D velocity components (solid lines). The energy transfer across the vacancy is greatest for positive  $\bar{v}_y$  and negative  $\bar{v}_z$  velocity components. (c) Selected top views from a DFT/MD trajectory of a higher-energy perpendicular ejection ( $\gamma = 5^\circ$ ,  $\delta = 5^\circ$ ,  $\vec{E}_n = 15$  eV) resulting in an N adatom near its original location.

“best” and “worst” case estimates for the true probability with the assumption that all migration barriers are equal. Based on 10 000 simulations for each case, probabilities for the N adatoms to recombine on the other side range from 32% (open world, only considering those atoms that do not escape) to 47% (periodic  $3 \times 3 \times 1$  cell). The latter value is used in Fig. 3 to plot the limiting case for the apparent jump cross sections via an adatom-mediated route.

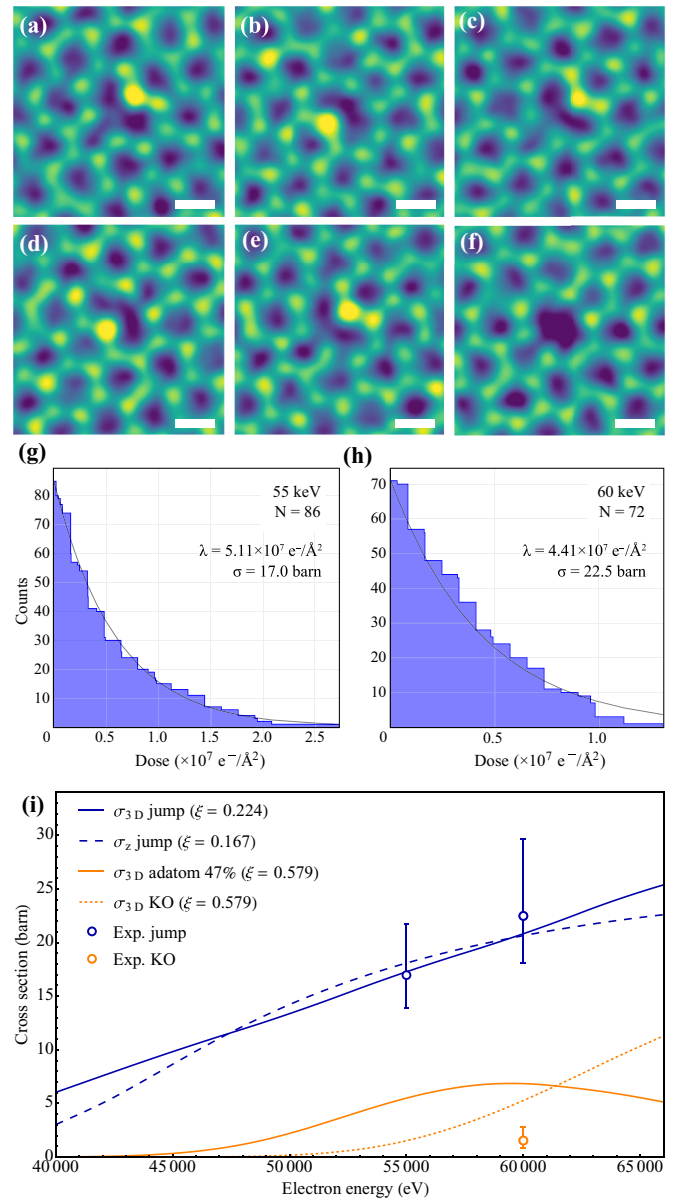


FIG. 3. Reversible jumps of N across a vacancy in graphene. (a)–(f) Six selected frames from a medium-angle annular dark-field scanning transmission electron microscopy image series, recorded at 60 keV at room temperature, which contained a total of 17 jumps, with the N atom finally ejected before the last frame. The scale bar is 2 Å. (g), (h) Exponential distribution of jump doses ( $N$  events in total; each bin contains all the events that occurred at doses higher than the lower bin limit) fitted with the expected Poisson expectation value  $\lambda$  at (g) 55 keV (resulting cross section  $\sigma$  of 17.0 barns) and (h) 60 keV (22.5 barns). (i) Comparison of experimental jump (blue open circles) and knock-on (KO; orange open circle) cross sections with the calculated ones for the full 3D (solid blue line) and  $z$ -only (dashed blue line) models for the direct jump pathway [Fig. 2(a)], as well as the 3D model for displacement to an adatom [example in Fig. 2(c)] followed by recombination on the other side at 47% probability (orange solid line), and direct knock-out corresponding to the same scaling factor  $\xi$  (orange dashed line). The error bars correspond to 2-sigma confidence intervals.

#### IV. COMPARISON TO EXPERIMENT ON PYRIDINIC NITROGEN

To test these predictions, we collected new room-temperature data on pyridinic N jumps at 55 and 60 keV by imaging incidental impurities identified by electron energy loss spectroscopy and obtained precise cross-section estimates (Fig. 3(i); [17]). Notably, the room-temperature value of 22.5 barns at 60 keV is slightly lower than the earlier rough estimate of 30 barns at 500 °C. We also observed eight knock-out events at 60 keV and estimated their cross section to be 1.54 barns. Finally, we explored including the variation of  $E_d$  due to thermal perturbations from the equilibrium geometry [14]. Unfortunately, the addition of an energy dimension to the integration of Eq. (4) proved numerically too demanding, nor is it possible to perform the required thermal sampling at our DFT/MD level of theory. However, this effect is expected to be a negligible correction [14].

In Table I we compare the  $z$ -only and 3D cross-section models, including the required scaling factor and the residual error of the simultaneous fit to experimental data points at different electron energies [13]. While the 3D model makes only a small difference for either of the cases that can be activated at emissions close to normal incidence (damage of pristine graphene and N adatom creation at the N-C<sub>2</sub> site), for the direct jump the required rescaling is somewhat smaller (factor  $\xi$  increased from 0.167 to 0.224). However, any elastic model cannot explain the remarkably high experimentally observed jump rates: without the scaling factor  $\xi$ , the predicted rate would be negligible at these electron energies, while the N atoms are observed to jump many times per minute.

Since the adatom-mediated route can be effectively activated with energy transfers closer to the plane normal, the scaling factor  $\xi$  required to describe the correct order of magnitude of the measured cross sections is closer to unity, but still quite substantial. Thus, theoretically calculated elastic threshold energy values would still predict a negligible probability for this process. Further, assuming that the N is recaptured on the opposite side of the vacancy 47% of the time, it is not possible to simultaneously explain the high probability of jumps and the relatively low probability of knocking out the N. In Fig. 3(i), the theoretical adatom and knock-on curves are simultaneously fitted to the jump and knock-out cross sections; a much lower  $\xi$  could push the cross section higher, but would result in a far too high probability of knocking out atoms.

Measurements at additional beam energies would be useful, but would not alter the general magnitude of the discrepancy. We also note that there will be a limited range of primary beam energies where (1) atomic resolution can be retained, (2) the process is fast enough to measure with sufficient statistics, and (3) competing processes such as knock-on

damage do not interfere. In our instrument, it is challenging to retain sufficient resolution at 50 keV, while the probability of knock-on damage at 65 keV and above may prevent the collection of robust statistics at higher energies.

#### V. CONCLUSION

Since vibrations in all directions and the variation of  $E_d$  as a function of emission angle are now accounted for in our complete theory, remaining discrepancies between simulated and experimentally derived values suggest an additional source: the inaccuracy of DFT/MD in describing the energy required to displace the N atom from the N-C<sub>2</sub> site within the ground-state Born-Oppenheimer approximation. Inelastic effects have been shown to be vital for explaining damage in nonmetallic 2D materials [10,27–30], but it is surprising they should also play such a role for point defects in metallic graphene. Recent theoretical work has proposed potential mechanisms and avenues for quantitative modeling [31]: further advances, building upon the 3D foundation established here, will be needed before a full quantitative picture can be drawn.

Finally, it may be instructive to consider the magnitudes of the energy barriers that the fitted  $\xi$  result in. A value of 0.224 brings a DFT/MD threshold energy of 13.0 eV down to less than 3 eV—still too large to be thermally activated, but below the calculated barrier of the in-plane minimum-energy pathway. Applying the same factor to that barrier would bring its value from 4 eV [26] down to as little as 0.9 eV—which could easily be crossed thermally. Considering the complexities of the analysis, these factors should not be taken as any direct measure of the effects of potentially complex dynamics driven by electronic excitations, but the magnitudes involved could suggest that the observed rates may be the result of lowering of thermal migration barriers due to inelastic electron scattering, which future theoretical developments may be able to directly quantify.

#### ACKNOWLEDGMENTS

A.C., A.M., and T.S. were supported by the European Research Council (ERC) under the European Union’s Horizon 2020 research and innovation program (Grant Agreement No. 756277-ATMEN), M.T. by the Austrian Science Fund (FWF) via Project No. P 28322-N36, and N.A.P. and M.J.V. by the Belgian Fonds National de la Recherche Scientifique (FNRS) under Grant No. T.0103.19-ALPS, and ULiège and the Fédération Wallonie-Bruxelles (ARC DREAMS G.A. 21/25-01). We acknowledge computational resources by the Vienna Scientific Cluster (VSC) and by the Consortium des Equipements de Calcul Intensif (CECI), funded by FRS-FNRS G.A. 2.5020.11; and the Zenobe Tier-1 supercomputer funded by the Walloon Government G.A. 1117545.

[1] P. W. Hawkes, *Philos. Trans. R. Soc. A* **367**, 3637 (2009).

[2] R. F. Egerton, *Micron* **119**, 72 (2019).

[3] F. Banhart, *Rep. Prog. Phys.* **62**, 1181 (1999).

[4] J. C. Meyer, C. Kisielowski, R. Erni, M. D. Rossell, M. F. Crommie, and A. Zettl, *Nano Lett.* **8**, 3582 (2008).

[5] J. Kotakoski, J. C. Meyer, S. Kurasch, D. Santos-Cottin, U. Kaiser, and A. V. Krasheninnikov, *Phys. Rev. B* **83**, 245420 (2011).

[6] T. Susi, J. Kotakoski, D. Kepaptsoglou, C. Mangler, T. C. Lovejoy, O. L. Krivanek, R. Zan, U. Bangert, P. Ayala,

- J. C. Meyer, and Q. Ramasse, *Phys. Rev. Lett.* **113**, 115501 (2014).
- [7] T. Susi, J. Meyer, and J. Kotakoski, *Ultramicroscopy* **180**, 163 (2017).
- [8] O. Dyck, S. Kim, S. V. Kalinin, and S. Jesse, *Appl. Phys. Lett.* **111**, 113104 (2017).
- [9] M. Tripathi, A. Mittelberger, N. A. Pike, C. Mangler, J. C. Meyer, M. J. Verstraete, J. Kotakoski, and T. Susi, *Nano Lett.* **18**, 5319 (2018).
- [10] T. Susi, J. C. Meyer, and J. Kotakoski, *Nat. Rev. Phys.* **1**, 397 (2019).
- [11] J. C. Meyer, F. Eder, S. Kurasch, V. Skakalova, J. Kotakoski, H. J. Park, S. Roth, A. Chuvilin, S. Eyhusen, G. Benner, A. V. Krasheninnikov, and U. Kaiser, *Phys. Rev. Lett.* **108**, 196102 (2012).
- [12] R. Egerton, *Microsc. Microanal.* **19**, 479 (2013).
- [13] T. Susi, C. Hofer, G. Argentero, G. T. Leuthner, T. J. Pennycook, C. Mangler, J. C. Meyer, and J. Kotakoski, *Nat. Commun.* **7**, 13040 (2016).
- [14] A. I. Chirita Mihaila, T. Susi, and J. Kotakoski, *Sci. Rep.* **9**, 12981 (2019).
- [15] T. Susi, D. Kepaptsoglou, Y.-C. Lin, Q. Ramasse, J. C. Meyer, K. Suenaga, and J. Kotakoski, *2D Mater.* **4**, 042004 (2017).
- [16] Y.-C. Lin, P.-Y. Teng, C.-H. Yeh, M. Koshino, P.-W. Chiu, and K. Suenaga, *Nano Lett.* **15**, 7408 (2015).
- [17] See Supplemental Material at <http://link.aps.org/supplemental/10.1103/PhysRevB.105.235419>, containing additional references [32–38], for the detailed derivation of the 3D energy transfer, the calculated phonon density of states, and the resulting atomic velocities for the N-C<sub>2</sub> site, detailed description of the theoretical cross-section calculation, details on the multidimensional numerical integration including the Wolfram *Mathematica* computational notebook, and a description of the analysis of experimental cross sections.
- [18] T. Susi, J. Kotakoski, R. Arenal, S. Kurasch, H. Jiang, V. Skakalova, O. Stephan, A. V. Krasheninnikov, E. I. Kauppinen, U. Kaiser, and J. C. Meyer, *ACS Nano* **6**, 8837 (2012).
- [19] A. H. Larsen, J. J. Mortensen, J. Blomqvist, I. E. Castelli, R. Christensen, M. Dułak, J. Friis, M. N. Groves, B. Hammer, C. Hargus, E. D. Hermes, P. C. Jennings, P. B. Jensen, J. Kermode, J. R. Kitchin *et al.*, *J. Phys.: Condens. Matter* **29**, 273002 (2017).
- [20] J. Enkovaara, C. Rostgaard, J. J. Mortensen, J. Chen, M. Dulak, L. Ferrighi, J. Gavnholt, C. Glinsvad, V. Haikola, H. A. Hansen, H. H. Kristoffersen, M. Kuisma, A. H. Larsen, L. Lehtovaara, M. Ljungberg *et al.*, *J. Phys.: Condens. Matter* **22**, 253202 (2010).
- [21] J. P. Perdew, K. Burke, and M. Ernzerhof, *Phys. Rev. Lett.* **77**, 3865 (1996).
- [22] A. Zobelli, A. Gloter, C. P. Ewels, G. Seifert, and C. Colliex, *Phys. Rev. B* **75**, 245402 (2007).
- [23] N. F. Mott and H. Massey, *The Theory of Atomic Collisions*, 3rd ed. (Clarendon Press, Oxford, 1965).
- [24] W. A. McKinley Jr. and H. Feshbach, *Phys. Rev.* **74**, 1759 (1948).
- [25] F. Seitz and J. S. Koehler, in *Solid State Physics*, Vol. 2 (Academic Press, New York, 1956), p. 305.
- [26] R. Arenal, K. March, C. P. Ewels, X. Rocquefelte, M. Kociak, A. Loiseau, and O. Stéphan, *Nano Lett.* **14**, 5509 (2014).
- [27] J. Kotakoski, C.H. Jin, O. Lehtinen, K. Suenaga, and A.V. Krasheninnikov, *Phys. Rev. B* **82**, 113404 (2010).
- [28] R. Zan, Q. M. Ramasse, R. Jalil, T. Georgiou, U. Bangert, and K. S. Novoselov, *ACS Nano* **7**, 10167 (2013).
- [29] G. Algara-Siller, S. Kurasch, M. Sedighi, O. Lehtinen, and U. Kaiser, *Appl. Phys. Lett.* **103**, 203107 (2013).
- [30] S. Kretschmer, T. Lehnert, U. Kaiser, and A. V. Krasheninnikov, *Nano Lett.* **20**, 2865 (2020).
- [31] D. B. Lingerfelt, T. Yu, A. Yoshimura, P. Ganesh, J. Jakowski, and B. G. Sumpter, *Nano Lett.* **21**, 236 (2021).
- [32] A. H. Romero, D. C. Allan, B. Amadon, G. Antonius, T. Applencourt, L. Baguet, J. Bieder, F. Bottin, J. Bouchet, E. Bousquet, F. Bruneval, G. Brunin, D. Caliste, M. Côté, J. Denier *et al.*, *J. Chem. Phys.* **152**, 124102 (2020).
- [33] D. R. Hamann, *Phys. Rev. B* **88**, 085117 (2013).
- [34] M. J. v. Setten, M. Giantomassi, E. Bousquet, M. J. Verstraete, D. R. Hamann, X. Gonze, and G.-M. Rignanese, *Comput. Phys. Commun.* **226**, 39 (2018).
- [35] C. Lee and X. Gonze, *Phys. Rev. B* **51**, 8610 (1995).
- [36] A. R. Krommer and C. W. Ueberhuber, *Computational Integration* (SIAM, Philadelphia, 1998).
- [37] Wolfram Research Inc., *Mathematica*, Version 12.3.1, 2021.
- [38] T. Susi, T. P. Hardcastle, H. Hofsäss, A. Mittelberger, T. J. Pennycook, C. Mangler, R. Drummond-Brydson, A. J. Scott, J. C. Meyer, and J. Kotakoski, *2D Mater.* **4**, 021013 (2017).